Effect of Z-Yarns on the Stiffness and Strength of Three-Dimensional Woven Composites

M.P. Rao, B.V. Sankar† and G. Subhash
Department of Mechanical and Aerospace Engineering
University of Florida
PO Box 116250 Gainesville, FL 32611-6250

(Accepted for publication in *Composites B: Engineering*)

ABSTRACT

Micromechanics tools investigating the in-plane elastic and strength properties of 3D woven composites are developed in this work. Particular attention is directed toward constructing detailed geometry and finite element models of an example 3D weave architecture available in the literature. The models are then modified to investigate the effect of including the Z-yarns on the changes in stiffness and strength properties. In particular, the effect of incorporating the 'Z-Crowns' is quantified with the aid of three-dimensional finite element simulations.

Keywords: 3D woven composite, finite element modeling, micromechanics, stiffness, strength.

INTRODUCTION

Traditional laminated, woven and braided composite materials are inherently susceptible to inter-layer delamination due to their micro-structural geometry and intrinsically weak inter-laminar bonds. Specifically, in hard armor applications, candidate composites should possess high areal density, superior delamination resistance and high fracture toughness. Three-dimensional (3D) woven composites are a class of materials that encompass all of the above mentioned properties. The micro-structural geometry of 3D woven composites is characterized by several layers of [0/90] laminates '*bound*' together with the aid of warp weavers or Z-yarns.

In practice however, the [0/90] laminates are integrally woven with Z-yarns, resulting in the model architecture shown in Figure 1. This process imparts favorable mechanistic characteristics such as high in-plane and through-thickness stiffness and strength, superior delamination resistance and high fracture toughness. Consequently, it becomes imperative to quantify the effect of integral Z-weaving on the stiffness, strength and fracture properties of 3D woven composites.

Several researchers [1 – 11] have investigated various aspects of the response of 3D woven composites in different environments. Elastic properties, strength, ductility and fatigue life of 3D woven composites [1] were experimentally determined to be highly sensitive to tow waviness. It should be noted here that 3D woven fabrics are not characterized by tow undulations similar to those witnessed in plain and satin weave fabrics. Tow waviness in [1] refers to sporadic undulations of nominally straight tows. As such, tow undulations have not been neglected in

†Corresponding author:
E-mail: sankar@ufl.edu Phone: (352) 392 6749 (Work)

Figure 1, but rather, the presented architecture approximates an actual 3D woven system [2]. The complete stress-strain response of 3D woven composites under quasi-static loads was experimentally characterized in [2], wherein tow waviness was not evident in the reported micrographs.

Fracture of 3D woven Carbon/Epicote 828 epoxy resin composites in [3] was linked to tow/matrix debonding, tow breakage, and fiber pull-out. The studies in [3] also confirmed the observations regarding mechanical properties of 3D woven composites reported in [1]. In a more general sense, mode-I inter-laminar fracture toughness and delamination resistance of 3D woven composites [4] was shown to significantly improve with relatively small volume fractions of Z-yarns.

From a manufacturing standpoint, the experimental characterization in [5] and [6] brought to light severe knockdowns in the strength of dry load bearing and uni-directional composite yarns. Abrasion damage caused by the fibers sliding against each other and the loom machinery was cited as the major contributor toward the degradation in strength properties.

Performance of 3D woven composites under impact loads was the main focus of studies in [7,8,9]. In general, 3D woven composites appear to have better ballistic efficiency, and controlled delamination as opposed to 2D woven composites [7] and as such incorporate better energy transfer characteristics [9].

Analytical work [2,10,11] has mainly focused on predicting the stiffness and strength of 3D woven composites. Homogenized "3D Mosaic" [2] and iso-stress/iso-strain based micro-mechanics models [10,11] tend to overestimate the properties since they are unable to account for localized events such as yarn micro-bending. Computational modeling on the other hand [8,9,11] can incorporate the three-dimensional stress state, without making any simplifying assumptions. However, in [8,9,11], the authors neglected Z-Crowns [2] (see also Figure 1), perhaps leading to a stiffer response.

The spectrum of works cited above, while not exhaustive, suggest that tow waviness [1,3,11], abrasion damage due to weaving [5,6], and introduction of Z-yarns [4,7] are primary factors that significantly influence the mechanics of 3D composites. Potential applications of 3D woven composites in critical environments such as vehicle armor motivate their complete in-plane and through-thickness characterization under static, rate-sensitive and dynamic loads.

However, the present study focuses on investigating the effect of Z-yarns on the in-plane elastic properties and strength of a model 3D woven composite system shown in Figure 1 with the aid of finite element based generalized micromechanics tools. The generality of the tools developed herein would lend itself for application to any particular woven system. Future studies as part of this broad research program would report on other aspects of the response of 3D woven composites mentioned above.

GEOMETRIC AND FINITE ELEMENT MODELING OF 3D WOVEN COMPOSITES

Modeling the geometry

The accurate prediction of the response of these materials under different loading environments mandates a detailed representation of their 3D weave architecture. Extension of modeling strategies developed in [12,13] to study 3D composites is not a trivial matter, simply because plain and satin weave textile composites are relatively two-dimensional (2D) when compared with material systems such as those depicted in Figure 1. As such in this study, the commercially available ABAQUS® finite element software is employed for developing solid models and corresponding finite element meshes of the unit-cell of the material system shown in Figure 1.

Figures 1(a) – (b) serve to present schematic representations of the weave architecture and isolate a repeating unit-cell that captures the periodicity of this textile composite. As shown in Figure 1(c), a coordinate system *XYZ* is established with its origin located at the geometric center of the repeating unit-cell, such that it constitutes the global coordinate system. Consistent with the definition of *XYZ*, the warp and fill tows constitute the planar 0^o (longitudinal) and 90^o (transverse) tows, respectively. The out-of-plane undulating fiber bundles are called Z-yarns.

Micrographs of processed 3D composites indicate a thin layer of matrix material above and below the Z-Crowns [3]. As such in the model simulations, a thin sliver of additional matrix material is introduced as shown in Figure 1(c) with $\delta_z = 0.1 * h_z$. The undulating path of the Z-yarns has been assumed to be regular and the tow cross-sections have been assumed to be uniform rectangles in the present study. Particular geometry parameters employed to model the material system in Figure 1 are reported in Table 1. Consequently, the total height of the unit-cell is given by:

$$H_{UC} = H + \delta_z \tag{1}$$

The geometric modeling strategy developed herein comprises of defining suitable volumetric partitions to represent the warp and fill tows, Z-yarns, and matrix material, within a cuboid of dimensions $L \times W \times H_{UC}$. The transversely isotropic tows and yarns, defined via partitioning, are then associated with appropriate local material directions as illustrated in Figures 2(a) – (b). The remaining volume of the cuboid is designated as the isotropic inter-tow epoxy resin matrix depicted in Figures 2(a) – (b).

In this study, two different configurations of the unit-cell in Figure 1(c) are modeled. The first configuration, which includes the Z-Crowns is designated 'Z-Crowned Composite' and shown in Figure 2(a). In the second configuration, the Z-Crowns are neglected consistent with [2,9]; this arrangement is termed 'Uncrowned Composite' as shown in Figure 2(b). Due to the particular geometry, the overall height of the unit-cell in this case is given by:

$$H_{UCC} = H - 2h_z \tag{2}$$

All other dimensions are the same as those reported in Table 1.

The material system in Figure 1 comprises of three layers of fill tows and two layers of warp tows integrally woven with Z-yarns. The volume fraction of the Z-yarns varies between 1% and 3%, and as such, the material is similar to a [0/90] stacked laminate, except for the presence of the Z-yarns and the matrix material. As such, the mechanistic limiting case of this configuration is an 'Equivalent Laminate' as shown in Figure 2(c). The overall height of the Equivalent Laminate is $H_{LAM} = H_{UCC}$. In Equation (2) and the above discussion, the subscripts '*UCC*' and '*LAM*' indicate Uncrowned Composite and Equivalent Laminate, respectively.

Finite element discretization

The solid models of the unit-cells shown in Figures 2(a) – (c), were meshed with 3D eight-node linear continuum brick elements within ABAQUS. A structured meshing algorithm was utilized such that the individual finite elements were characterized by regular hexahedral geometry. Consequently distorted elements were altogether eschewed as part of the meshing process. The partition-feature based modeling methodology described earlier, results in merged interfaces at material boundaries. Therefore, while meshing, duplicate or coincident nodes are not generated at these interfaces. As such, additional constraints for coincident nodes and node merging operations at material boundaries are completely avoided.

Boundary conditions

Exploiting the periodicity of the woven architecture in 3D composites, appropriate periodic boundary conditions were specified on the four vertical faces of the unit-cells corresponding to $X = \pm a/2$ and $Y = \pm b/2$. The unit-cells faces located at $Z = \pm c/2$ were set free. The generalized dimensions 'a', 'b', and 'c', are reported in Figure 2(d). In particular, the following relations are implied for 'a', 'b', and 'c':

$$\begin{aligned} a &= L \\ b &= W \\ c &= \begin{cases} H_{UC} + \delta_z \rightarrow Z - Crowned\ Composite \\ H_{UCC} \rightarrow Uncrowned\ Composite \\ H_{LAM} \rightarrow Equivalent\ Laminate \end{cases} \end{aligned} \tag{3}$$

Periodic boundary conditions simulating remote in-plane tension and shear are reported in Table 2. Detailed discussions regarding the derivation of these boundary conditions are presented elsewhere [14].

Constituent material properties

The transversely isotropic fill tows, warp tows and Z-yarns were intrinsically S-2 Glass/Dow Derakane 8084 Vinyl-Ester unidirectional composites, with material properties listed in Table 3. The isotropic epoxy resin matrix was characterized by elastic modulus, $E = 3.53$ GPa, Poisson's ratio, $\nu = 0.35$, and yield strength, $S_y = 125$ MPa.

MECHANICS OF 3D WOVEN COMPOSITES

The Direct Micro-Mechanics (DMM) techniques discussed in [14] are employed herein to develop generalized finite element method based approaches to predicting the in-plane effective elastic properties and strengths of 3D woven composites. Computation of the extensional stiffness [A], bending-extension coupling stiffness [B] and the bending stiffness [D] matrices is central to the above methods. A general algorithm would be presented later toward the end of this section.

Unlike the meso-volume based 3D-Mosaic [2] and analytical [10,11] models, the DMM technique allows one to capture the effects of geometric details leading to critical mechanistic events, such as yarn micro-bending. As such, this method better approximates the response of 3D woven composites. Especially while addressing non-linear rate-sensitive, impact and ballistic loading response of these advanced materials, 3D finite element models incorporating micro-structural geometric details have to be developed.

In-Plane Effective Elastic Properties of 3D Woven Composites

Following the discussions in [14] it could be shown that, in the absence of bending-extension coupling and applied moments, the in-plane resultant forces are given by:

$$\begin{Bmatrix} N_x \\ N_y \\ N_{xy} \end{Bmatrix} = [A] \begin{Bmatrix} \varepsilon_x \\ \varepsilon_y \\ \gamma_{xy} \end{Bmatrix} \tag{4}$$

Furthermore, the equivalent stiffness matrix $[Q]$ of the woven/stitched composite laminate referred to the global coordinate system could be computed as,

$$[Q] = [A]/h \tag{5}$$

wherein 'h' is the overall height of the laminate. Once the $[Q]$ matrix has been determined, the effective elastic properties of the composite could be computed as:

$$\begin{Bmatrix} E_{xx} \\ E_{yy} \\ G_{xy} \\ \nu_{xy} \\ \nu_{yx} \end{Bmatrix} = \Delta \begin{Bmatrix} Q(1,1) \\ Q(2,2) \\ Q(3,3)/\Delta \\ Q(1,2)/\Delta Q(2,2) \\ Q(1,2)/\Delta^2 Q(1,1) \end{Bmatrix} \tag{6}$$

In Equation (6):

$$\Delta = 1 - \frac{Q(1,2)^2}{Q(2,2)Q(1,1)} \tag{7}$$

Predicting the In-Plane Strength of 3D Woven Composites

The broader problem in predicting the strength of 3D woven composites focuses on computing a load factor for the composite under a general state of in-plane loading represented by $\{\sigma\} = \{\sigma_x\ \sigma_y\ \tau_{xy}\}^T$. However, in this case, the constitutive [*A*] matrix is related to the resultant forces as described in Equation (4). Therefore the above problem could be restated as involving the computation of a load factor for the composite under a given state of in-plane loading described by $[N] = \left[N_x\ N_y\ N_{xy}\right]^T$.

The approach is based on computing load factors under five unique loading conditions given by:

$$\begin{Bmatrix} N_{L(+)} \\ N_{L(-)} \\ N_{T(+)} \\ N_{T(-)} \\ N_{LT} \end{Bmatrix} = \begin{Bmatrix} 1 & 0 & 0 \\ -1 & 0 & 0 \\ 0 & 1 & 0 \\ 0 & -1 & 0 \\ 0 & 0 & 1 \end{Bmatrix} \tag{8}$$

From Equation (8), $N_{L(+)} = \{1\ 0\ 0\}^T$ would represent a unit tensile load in the Longitudinal (*L*) or 0°-direction of the composite. Similarly, $N_{L(-)} = \{-1\ 0\ 0\}^T$ would indicate a unit compressive load in the *L*-direction of the composite. $N_{T(+)} = \{0\ 1\ 0\}^T$ and $N_{T(-)} = \{0 - 1\ 0\}^T$ have corresponding connotations albeit in the transverse (*T*) or 90°-direction of the composite. $N_{LT} = \{0\ 0\ 1\}^T$ indicates a unit shear load parallel to the *L* – *T* plane of the composite.

Computing total stress

For any given in-plane loading state [*N*] determined from Equation (8), the corresponding macro-strains $\{\varepsilon\}$ are computed with the aid of Equation (4). Employing the principle of linear superposition, and the macro-strains $\{\varepsilon\}$, the total stress vector in each element of the finite element mesh is computed as:

$$\{\sigma^{xyz}\}^e_{Total} = \varepsilon_x\{\sigma\}^e_{XX} + \varepsilon_y\{\sigma\}^e_{YY} + \gamma_{xy}\{\sigma\}^e_{XY} \tag{9}$$

The 6×1 vectors $\{\sigma\}^e_{XX}$, $\{\sigma\}^e_{YY}$ and $\{\sigma\}^e_{XY}$ in Equation (9) correspond to the micro-stresses in each element as a result of the three individual macro-level unit-strain loading cases listed in

Table 2. The subscripts '*XX*', '*YY*' and '*XY*' refer to unit-strain in the *X*-direction, *Y*-direction and *XY*-shear, respectively.

For checking failure, the material code of the particular element '*e*' is determined to indicate whether it resides within the fill tows, warp tows, Z-yarns or the inter-tow epoxy resin matrix. If the element '*e*' resides within a tow, then consistent with [14], the total stress is transformed to the corresponding local 1-2-3 coordinate system:

$$\{\sigma^{123}\}^e_{Total} = [T]\{\sigma^{xyz}\}^e_{Total}[T]^T \tag{10}$$

In Equation (10), [T] is the transformation matrix of direction cosines resulting from appropriate coordinate rotations, and the superscript 'T' indicates transpose of [T]. The total stress $\{\sigma^{xyz}\}^e_{Total}$ is not subject to any transformations if 'e' resides in the inter-tow epoxy resin matrix.

Load factor based on the Tsai-Hill failure criterion

Under plane stress conditions parallel to the 1-2 plane, with the fiber direction being aligned along the 1-direction, the Tsai-Hill failure criterion is given by (Jones [15]):

$$\frac{\sigma_{11}^2}{X^2} - \frac{\sigma_{11}\sigma_{22}}{X^2} + \frac{\sigma_{22}^2}{Y^2} + \frac{\tau_{12}^2}{S^2} = 1 \tag{11}$$

In Equation (11), $\{\sigma\} = \{\sigma_{11}\ \sigma_{22}\ \tau_{12}\}^T$ represent a particular planar loading state, and X, Y, and S are the in-plane longitudinal, transverse and shear strengths of the composite, respectively. Appropriate magnitudes of $X = X_t$ and $X = X_c$ and $Y = Y_t$ or $Y = Y_c$ should be used depending on the signs of σ_{11} and σ_{22}. In the above, subscripts 't and 'c' imply tension and compression, respectively. Therefore, if σ_{11} is positive, $X = X_t$ and if it is negative, $X = X_c$. Similarly, positive σ_{22} requires $Y = Y_t$ and negative σ_{22} implies $Y = Y_c$.

Let λ be the load factor for a given material under unit tensile load. Further let the planar stresses corresponding to the unit tensile load case be s_{11}, s_{22} and s_{12}. The condition $\lambda > 1$ implies that the material can withstand stresses of magnitude λs_{11}, λs_{22}, and λs_{12}. If the Tsai-Hill failure criterion is used to check for failure, $\sigma_{11} = \lambda s_{11}$, $\sigma_{22} = \lambda s_{22}$, and $\tau_{12} = \lambda s_{12}$ have to be substituted in Equation (11). As a result, the load factor is given by:

$$\lambda = \frac{1}{\sqrt{\frac{s_{11}^2}{X^2} - \frac{s_{11}s_{22}}{X^2} + \frac{s_{22}^2}{Y^2} + \frac{s_{12}^2}{S^2}}} \tag{12}$$

In this study, s_{11}, s_{22} and s_{12} appearing in Equation (12), are determined with the aid of Equation (10) as:

$$\begin{Bmatrix} s_{11} \\ s_{22} \\ s_{12} \end{Bmatrix} = \begin{Bmatrix} \sigma_{11}^{123} \\ \sigma_{22}^{123} \\ \sigma_{12}^{123} \end{Bmatrix}^e_{Total} \tag{13}$$

Load factor based on the maximum principal stress failure criterion

According to the maximum principal stress failure criterion, failure occurs if the maximum principal stress at a point in the material exceeds the yield strength of the material.

Let us assume s_1, s_2 and s_3 are the principal stresses corresponding to the three-dimensional stress state $\{\sigma\} = \{\sigma_{xx}\ \sigma_{yy}\ \sigma_{zz}\ \tau_{xy}\ \tau_{yz}\ \tau_{zx}\}^T$ resulting from a unit tensile load. Furthermore, let S_y represent the yield strength of the material. If λ is the load factor for this load case, then the

condition $\lambda > 1$ implies that the material can actually withstand stresses of the magnitude $\lambda\{\sigma\}$. As a result, the principal stresses would be λs_1, λs_2, λs_3. Invoking the maximum principal stress failure criterion $\max(\lambda s_1, \lambda s_2, \lambda s_3) \geq S_y$, the load factor could be computed as:

$$\lambda = \frac{S_y}{\max\left(|s_1|, |s_2|, |s_3|\right)} \tag{14}$$

Strength computations based on the 'One Element' condition

Load factors for tow elements are computed from Equation (12), whereas Equation (14) is used to determine load factors for matrix elements. The minimum load factor for the finite element determines the corresponding strength of the composite, for each loading case. For instance,

$$S_{L(+)}^{FEA} = \frac{\min\left(\lambda^e\right)}{h} \tag{15}$$

indicates the longitudinal tensile strength of the composite corresponding to the load case $N_{L(+)} = \{1\ 0\ 0\}^T$. The subscript '$L(+)$' represents tension in the longitudinal direction. The superscript '*FEA*' implies that the strength is computed based on stress estimates obtained from the finite element boundary value problems listed in

Table 2. Also in Equation (15), λ^e is the element load factor and 'h' is the overall height of the composite, given by 'c' in Equation 3.

Similarly, $S_{L(-)}^{FEA}$, $S_{T(+)}^{FEA}$, $S_{T(-)}^{FEA}$, and S_{LT}^{FEA} could be determined for the remaining four loading cases in Equation (8). In the above, subscript '(–)' indicates compression, and superscript '*T*' refers to the transverse direction.

The strength magnitudes determined above are the most conservative estimates since one element in the entire mesh dictates the response of the composite. This approach to estimating strength is designated the 'One Element' condition. Later in this study, discussions focusing on relaxing the element failure threshold for computing the planar strengths would be presented.

Computing the Extensional Stiffness and Bending-Extension Coupling Matrices

The crux of implementing the procedures discussed above is the computation of the extensional stiffness matrix [*A*]. Following the discussions in [14,16], the constitutive matrices [*A*], [*B*], and [*D*] for a given composite material could be computed with the aid six fundamental macro-level unit-strain and unit-curvature finite element boundary value problems. In particular, each macro-level unit-strain and unit-curvature boundary value problem results in the determination of one column of the 6×6 stiffness matrix formulated from the [*A*], [*B*] and [*D*] matrices.

This study however, focuses on the in-plane extensional and shear response of 3D woven composites. As such, only the three periodic finite element boundary value problems listed in Table 2 would be solved. In each of these boundary value problems, all other macro-strains are set to zero. Pursuant to the discussions in [14,16], the solution of the above three boundary value

problems leads to the computation of the first three columns of the 6×6 stiffness matrix formulated from the [A], [B] and [D] matrices. In other words, the extensional stiffness matrix [A], and the bending-extension coupling matrix [B], are fully determined.

RESULTS

Deformed meshes

Figure 3 presents the deformed mesh configurations of the Z-Crowned Composite and Uncrowned Composite unit-cell configurations. Under the application of the macro-level unit-strain $\varepsilon_x = 1$, the Z-Crowned Composite exhibits significant micro-bending due to the undulating path of the Z-yarns, as shown in Figure 3(a). In fact, through the vertical portion of the Z-yarns, the load path is aligned along the plane comprising the weakest 2-3 local material directions. Consequently, visible bulging of the Z-yarns near the top 'Z-Crown' is seen in Figure 3(a). The same effect is observed near the bottom 'Z-Crown' as well.

However, in the case of the Uncrowned Composite shown in Figure 3(b), the localized micro-bending is not apparent, since the Z-Crowns have been neglected. Nonetheless, perceptible bulging of the included portion of the 'Z-yarns' is clearly discernible on account of the alignment of the load path discussed above.

Solutions corresponding to unit macro-strain loading cases $\varepsilon_y = 1$, and $\gamma_{xy} = 1$, do not exhibit such severe micro-bending, as reported in Figure 3. Overall, the solutions presented in Figure 3, appear to be mechanistically reliable.

Constituent matrices and effective elastic properties

The extensional stiffness matrix [A] and the bending-extension coupling stiffness matrix [B] were computed based on the approach discussed in the previous section. Table 4 reports on the results obtained via the finite element method and an analytical solution for a five-layer [0/90] laminate resembling the Equivalent Laminate shown in Figure 2(c). The analytical solution is based on Classical Lamination Theory as described in [15]. Comparing the solutions for the 'Five-Layer [0/90] Laminate' and Equivalent Laminate reinforces confidence in the approach developed in this study. All the solutions reported in Table 4 indicate that the off-diagonal terms [A_{16}] and [A_{26}] are zero implying that these materials do not exhibit any shear-extension coupling. Furthermore, owing to the geometric symmetry of these materials with respect to the mid-plane, the bending-extension coupling matrix [B] turns out to be [0].

Results for the Z-Crowned Composite and the Uncrowned Composite in Table 4 bring to light the detrimental effect of Z-yarns on the stiffness properties of 3D composites. Comparing the properties of the Equivalent Laminate in Table 4 and results from [2,9] reproduced in Table 5, it is yet again confirmed that introduction of Z-yarns results in stiffness knockdown. As further seen from Table 5, it is evident that the results of the present study agree well with published data.

Load factors and In-Plane strengths

In-plane strengths for the Z-Crowned Composite, Uncrowned Composite and the Equivalent Laminate, corresponding to the five loading cases in Equation (8) were computed as discussed in a previous section, and are reported in Figure 4. Additionally in Figure 4, the in-plane strength of the 'Five-Layer [0/90] Laminate' computed based on Classical Lamination Theory [15] under different loading cases is also reported. For each loading case, the first, second, third and fourth bars represent the corresponding strengths of the 'Five-Layer [0/90] Laminate', Equivalent Laminate, Uncrowned Composite, and the Z-Crowned Composite, respectively. Excellent agreement between the strengths computed for the 'Five-Layer [0/90] Laminate' and the Equivalent Laminate, inspire confidence in the methods developed in this study. Consistent with the stiffness properties of these material systems, the in-plane strengths also suffer significant knockdowns as a result of integral weaving with Z-yarns.

In order to relax the One Element failure condition, elements in the finite element mesh were grouped together on the basis of load factors, regardless of the material code. Distributions of the load factors for the first 15% of the elements in the Z-Crowned Composite and the Uncrowned Composite unit-cell finite element meshes are presented in Figure 5. The load factors for the first 15% elements in the Equivalent Laminate finite element mesh acquired unique constant magnitudes for individual loading cases, on account of its geometric and mechanistic homogeneity. The distributions in Figure 5 show that the load factors stabilize after about 1% of the elements are allowed to fail. Moreover, allowing either 5% or 10% elements to fail would be too liberal from the perspective of determining strength for a particular load case.

Based on load factors corresponding to 1%, 5% and 10% element failure, new strengths were computed for the Z-Crowned Composite and the Uncrowned Composite, for all the five loading cases, and are presented in Figure 6. The dashed horizontal lines in Figure 6 represent the strengths for the Equivalent Laminate, which as expected remain unaltered. To maintain clarity of the results presented in Figure 4 and Figure 6, the strength magnitudes of all the material systems corresponding to the One Element and 1% percent element failure criterion are listed in Table 6.

Changing the allowable element failure threshold, clearly affects the predicted strengths for the Z-Crowned Composite, and the Uncrowned Composite, as shown in Figure 6(a) and Figure 6(b), respectively. The percentage increase in the strengths of the Z-Crowned Composite, and the Uncrowned Composite for all five loading cases reported in Table 6, correspond to changing the element failure threshold from the One Element to the 1% element failure criterion. The longitudinal compressive strength of the Z-Crowned Composite is predicted to experience the most significant increase. On the other hand, maximum increase in strength for the Uncrowned Composite occurs under the transverse compression loading case. Further increases in allowable element failure thresholds to 5% and 10% element failure, do serve to push the predicted strengths toward those of the Equivalent Laminate, but these criteria are considered to be very liberal.

Pursuant to the above discussion, 1% allowable element failure threshold is now set as the criterion to choose the load factor for all the three material configurations, under any given state

of loading. Strength knockdowns resulting from the One Element and 1% allowable element failure threshold are presented in Figure 7. The first bar in Figure 7(a) – (b) corresponds to the Equivalent Laminate whereas the second and third bars represent in-plane strengths for the Uncrowned Composite and the Z-Crowned Composite, respectively. As the element failure threshold is increased, individual load factors decrease and the corresponding strength increases. Consequently, the percentage knockdown in strength decreases.

Failure loci

The in-plane strengths computed for the Z-Crowned Composite, Uncrowned Composite and the Equivalent Laminate, under the One Element and 1% element failure condition are reported in Table 6. Failure envelopes are then plotted based on the Tsai-Wu, Tsai-Hill, and Maximum Stress Theory criteria, using the strength values corresponding to the 1% element failure condition in Table 6.

Failure envelopes for the Z-Crowned Composite, Uncrowned Composite and the Equivalent Laminate, could be plotted for generalized load states $\{\sigma\} = \{\sigma_{xx}\ \sigma_{yy}\ \tau_{xy}\}$, by suitably varying the Euler angles ϕ and θ, shown in Figure 8. In particular, σ_{xx} and σ_{yy} are related as $\sigma_{yy} = \sigma_{xx}\tan(\phi)$ and failure loci are plotted by varying ϕ in the range $0 \leq \phi \leq 2\pi$. While using the Tsai-Hill failure criterion, X and Y (see Equation 11) are assigned appropriate magnitudes depending of the value of ϕ. For example, if $\frac{\pi}{2} \leq \phi \leq \pi$, then $X = -S_{L(-)}^{FEA}$ and $Y = S_{T(+)}^{FEA}$. Similarly, the appropriate sign of σ_{xx} is chosen depending on the magnitude of ϕ. The Tsai-Wu failure envelope on the other hand, is plotted consistent with the discussion in [17].

However, for the sake of brevity, failure loci shown in Figure 9, correspond to the case wherein $\theta = 0$, implying planar loading states given by $\{\sigma\} = \{\sigma_{xx}\ \sigma_{yy}\ 0\}$. Intersection of the individual failure envelopes with the coordinate axes represents longitudinal and transverse strengths for corresponding material configurations. Specifically, intersections in positive domains represent tensile strengths, whereas those on the negative domains of the coordinate axes correspond to compressive strengths, respectively. As seen from Figure 9, introduction of the Z-yarns results in significant knockdowns in the in-plane strengths. Furthermore in Figures 9(a) – (d), the small ellipse is placed merely to indicate the location of the origin.

DISCUSSION

Previous studies on these and other materials belonging to the family of woven composites [2 – 8,9,14,16], have shown that their mechanical behavior is intrinsically tied to the weave architecture. Finite element method based mechanistic studies therefore, require robust geometry models with the ability to capture the micro-structural architecture in great detail and sensitivity to adapt to changes in the same. The models developed herein while robust from the perspective of yielding reliable solutions, need to be refined to better approximate the path of the Z-yarns through the thickness of the composite.

One of the mechanistic effects of Z-yarns manifests itself as pronounced micro-bending discussed earlier. These micro-bending effects, while significant, are however, highly localized. In the bulk of the unit-cell, these local effects are negligible. Though the associated strain and stress gradients are localized, significant knockdowns in the effective properties are predicted as reported in Table 4 and Table 6. Therefore including the effects of Z-Crowns becomes imperative even in micro-mechanical analyses. By extrapolation then, Z-Crowns should be included in scenarios wherein inter-laminar delamination is expected. This might be the case in impact loading situations, since the very purpose of introducing Z-yarns in integrally woven 3D fabric composites is to contain delamination.

The strength results obtained as part of this study are compared with those reported in [2] and presented in Table 7. The 'Ref [2] – Theoretical' strength $S_{L(+)}$ is greater than the Uncrowned Composite strength $S_{L(+)}$ by 16% based on the results in Table 7
Table 7. However, the 'Ref [2] – Experimental' strength $S_{L(+)}$ is greater than the Z-Crowned Composite strength $S_{L(+)}$ by 36%. These variations could be attributed to differences in micro-structural geometry and boundary conditions imposed in the current study to simulate uni-axial tensile response.

Specifically, in case of the Uncrowned Composite, the volume fraction of warp and fill tows, and the Z-yarns was determined to be 48.65%, 37.16%, and 1.57%, respectively. However, for the Z-Crowned Composite the above volume fractions were 37.86%, 28.91% and 3.28%, respectively. These significant variations in volume fractions could be ascribed to differences in the actual and modeled micro-structural geometry – an observation consistent with [2]. Since the volume fractions for the Uncrowned Composite are closer to those reported in [2], the strengths presented in Table 7 for this case are in better agreement with the corresponding magnitudes from [2]. The discrepancy in the results obtained for the Z-Crowned Composite whose modeled architecture is much closer to real materials indicates that one should endeavor to construct better geometry models rather than neglect the Z-Crowns.

As seen from the results in Figure 9, the Tsai-Wu, Tsai-Hill and Maximum Stress Theory phenomenological failure criteria are unable to completely capture the behavior of 3D woven composites. These results indicate that 3D woven composites respond more like a structure rather than a material, when subjected to mechanical loading. Consequently, DMM techniques along with constrained optimization methods [18] to minimize the enclosed area of a failure ellipse or volume of a failure ellipsoid, are perhaps better suited to predict the strengths of 3D woven composites under a generalized loading state.

CONCLUSIONS

This study focused on investigating the effect of Z-yarns on the in-plane stiffness and strength of 3D woven composites. The tow materials were modeled as transversely isotropic, whereas the matrix material was regarded as an isotropic entity. Failure of the tows was assumed to be governed by the Tsai-Hill criterion, while the maximum principal stress condition was invoked to check for failure of the matrix material.

If only the through-thickness segments of the Z-yarns are included (Uncrowned Composite), the elastic moduli in the longitudinal (E_{xx}) and transverse (E_{yy}) directions are knocked down by approximately 16% and 10%, respectively. The knockdowns are computed with respect to the Equivalent Laminate which is a comparable 2D cross-ply laminate comprised of stacked [0/90] uni-directional laminas. However, if both the 0^o-oriented planar and through-thickness segments of Z-yarns are included (Z-Crowned Composite) then the above properties are knocked down approximately 30% and 24%, respectively. Similarly, the knockdown in the in-plane strengths of the material system investigated in this study is compared with data available in [2] and reported in

Table 8. As expected, the most severe knockdowns are predicted for the Z-Crowned Composite.

The Equivalent Laminate, Uncrowned Composite and the Z-Crowned Composite were found to stiffer in the longitudinal direction as compared with the transverse direction, as indicated by the result $E_{xx} > E_{yy}$ in Table 4. Consistently, the strengths in the longitudinal and transverse directions were characterized by the same relationship since $S_{L(+)}^{FEA} > S_{T(+)}^{FEA}$ and $S_{L(-)}^{FEA} > S_{T(-)}^{FEA}$ in Table 6. As expected, the Equivalent Laminate is much stronger in shear as compared reasonably well with both Uncrowned Composite and the Z-Crowned Composite, as reported in Table 6.

The mechanics approaches developed in this study are applicable to a broad range of woven composites [14,16]. This assertion is further attested by consistent stiffness results reported in Table 4 and Table 5 and strength results presented in Figure 4. Consistency of the above results stems from the fact that the finite element results for the Equivalent Laminate morphology are in excellent agreement with the comparable analytical 'Five-Layer [0/90] Laminate' layup.

On account of the solutions reported in Figure 3, Figure 4, Table 4, and Table 5, it is reasonable to conclude that these models and corresponding solutions are mechanistically reliable.

ACKNOWLEDGEMETS

The funding for this work was provided by the United States Army Research Office (grant number W911NF-08-1-0120), with Dr. Bruce LaMattina as the Program Manager and the United States Army Research Laboratory. The authors are grateful for the financial support.

REFERENCES

1. Cox, BN, Dadkhah, MS. Macroscopic elasticity of 3D woven composites. Journal of Composite Materials 1995;29(6): 785 – 819.
2. Bogdanovich, AE. Multi-scale modeling, stress and failure analyses of 3-D woven composites. Journal of Materials Science 2006;41:6547 – 6590.
3. Tan, P, Tong, L, Steven, GP, Ishikawa, T. Behavior of 3D orthogonal woven CFRP composites. Part I. Experimental investigation. Composites Part A 2000;31: 259 – 271.
4. Rudov-Clark, S, Mouritz, AP. Tensile fatigue properties of a 3D orthogonal woven composite. Composites Part A 2008;39: 1018 – 1014.
5. Lee, L, Rudov-Clark, S, Mouritz, AP, Bannister MK, Herszberg, I. Effect of weave damage on the tensile properties of three-dimensional woven composites. Composite Structures 2002;57: 405 – 413.
6. Rudov-Clark, S, Mouritz, AP, Lee, L, Bannister, MK. Fibre damage in the manufacture of advanced three-dimensional woven composites. Composites Part A 2003;34: 963 – 970.
7. Grogan, J, Tekalur, SA, Shukla A, Bogdanovich, A, Coffelt, A. Ballistic resistance of 2D and 3D woven sandwich composites. Journal of Composite Materials May 2007;9: 283 – 302.
8. Lv, L, Gu, B. Transverse impact damage and energy absorption three-dimensional orthogonal hybrid woven composite: experimental and FEM simulation. Journal of Composite Materials 2008;42(17): 1763 – 1786.
9. Gama BA, Haque, MdJ, Gillespie, Jr., JW, Bogdanovich, AE. In: CD Proceedings of 49th International SAMPE Symposium and Exhibition, May 16 – 24, 2004. SAMPE Publication, Long Beach, CA.
10. Naik, NK, Azad, NM Sk., Durga Prasad, P. Stress and failure analysis of 3D orthogonal interlock woven composites. Journal of Reinforced Plastics and Composites 2001;20(17): 1485 – 1523.
11. Tan, P, Tong, L, Steven, GP, Ishikawa, T. Behavior of 3D orthogonal woven CFRP composites. Part II. FEA and analytical modeling approaches. Composites Part A 2000;31: 273 – 281.
12. Kuhn JL, Charalambides, PG. Modeling of plain weave fabric composite geometry. Journal of Composite Materials 1999;33(3): 188 – 220.
13. Rao, MP, Pantiuk, M, Charalambides, PG. Modeling the geometry of satin weave fabric composites. Journal of Composite Materials 2009;43(1): 19 – 56.
14. Karkkainen, RL, Sankar, BV. A direct micro-mechanics method for analysis of failure initiation of plain weave textile composites. Composite Sciences and Technology 2006;66: 137 – 150.
15. Jones, RM. Mechanics of composite materials. Second Edition. Taylor and Francis, Inc, 1999.
16. Sankar, BV, Marrey, RV. Analytical method for micromechanics of textile composites. Composites Science and Technology 1997;57: 703 – 713.
17. Daniel, IM, Ishai, O. Engineering mechanics of composite materials. Oxford University Press, New York, USA, 1994.

18. Stamblewski, C, Sankar BV, Zankert, D. Analysis of three-dimensional quadratic failure criteria for thick composites using the direct micromechanics method. Journal of Composite Materials 2008;42(7): 635 – 654.

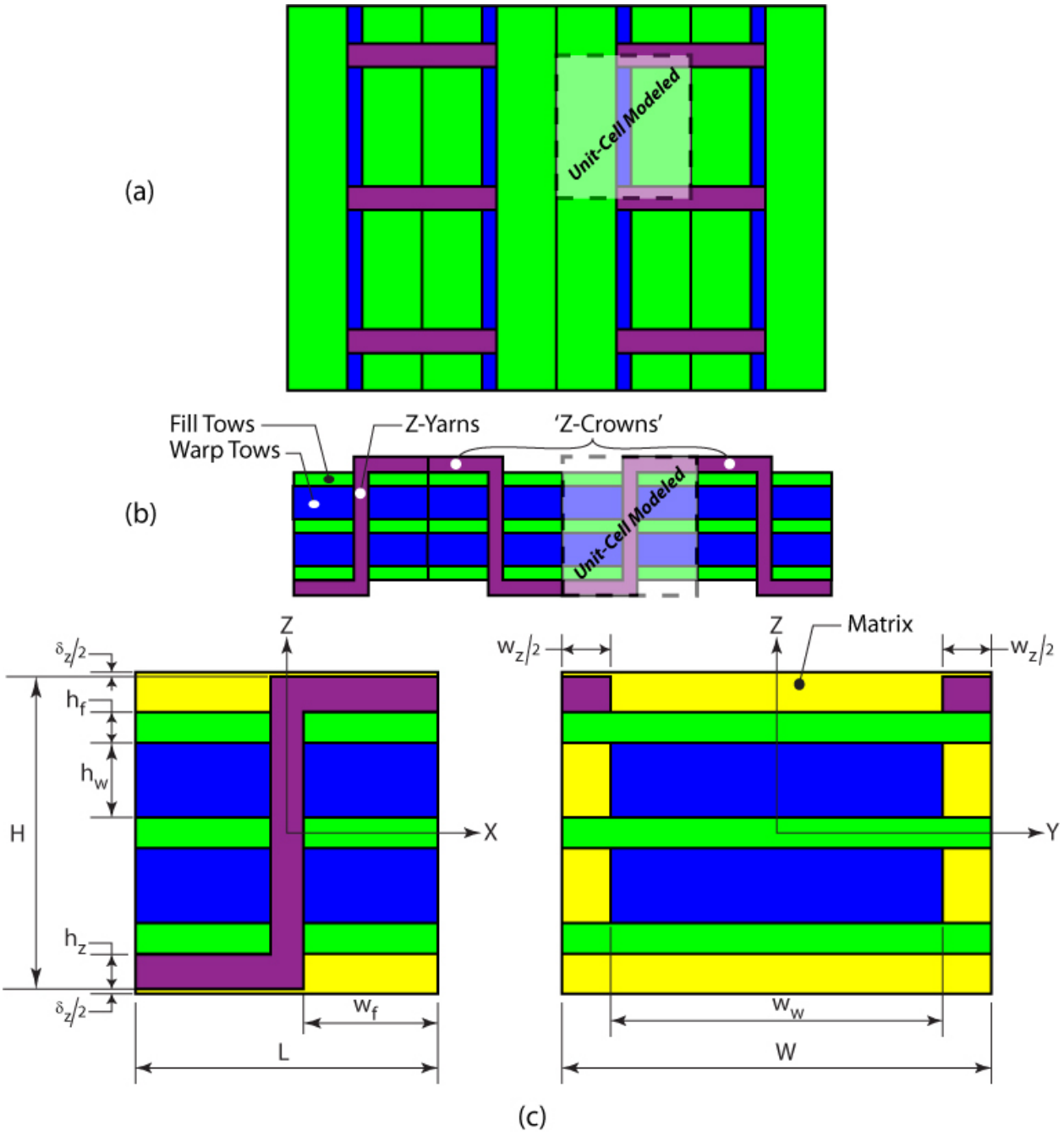

Figure 1: Schematic representation of the weave architecture in three-dimensional (3D) woven composites. The above schematics depict geometric modifications of the weave patterns

presented in [1]. (a) Plan view. (b) Front cross-sectional view exhibiting the path of the Z-Yarns. (c) Details of the unit-cell modeled in this study. The two views aid in completely identifying all the geometry parameters used to develop 3D finite element models of the unit-cell.

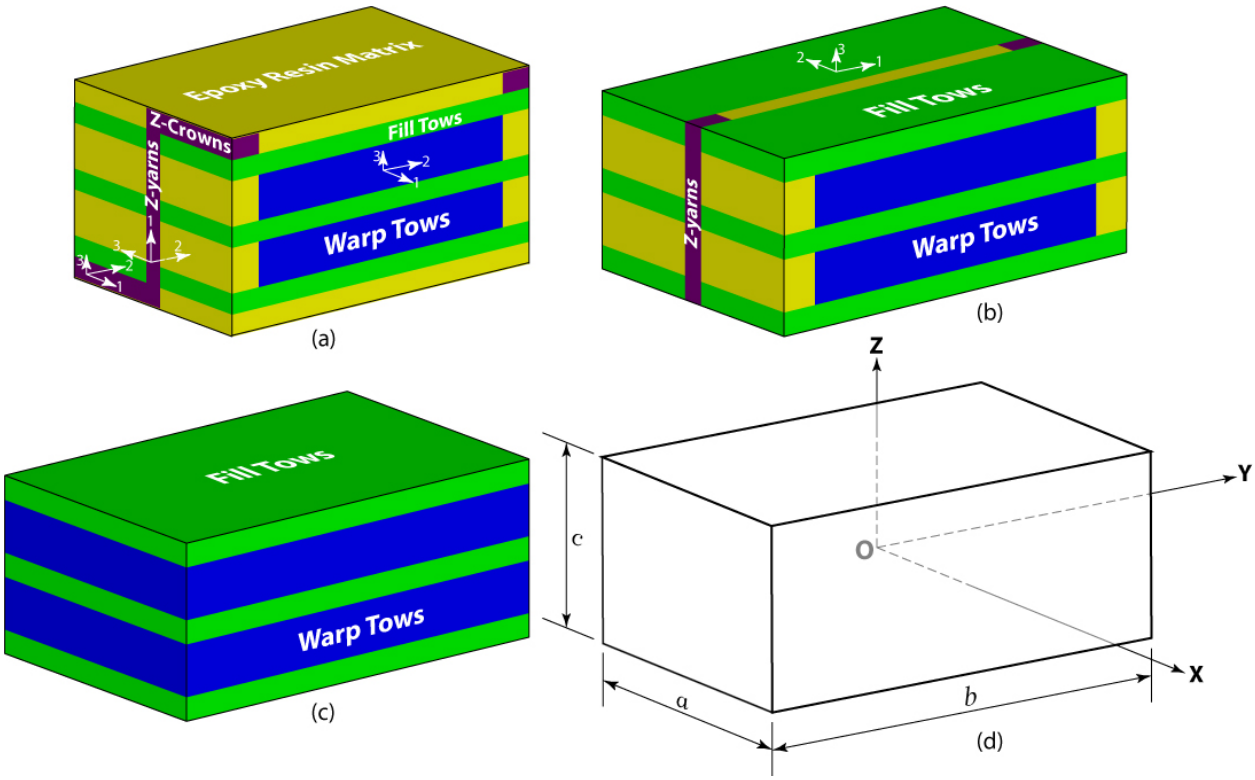

Figure 2: 3D solid models and dimensions of the unit-cell configurations modeled in this study. (a) Z-Crowned Composite exhibiting the arrangement of warp tows, fill tows and the out-of-plane Z-Yarns, along with the corresponding Principal Material Directions (PMDs). (b) Uncrowned Composite exhibiting PMDs of fill tows. (c) Equivalent Laminate. (d) Generalized unit-cell displaying the overall dimensions and the global *XYZ* coordinate system.

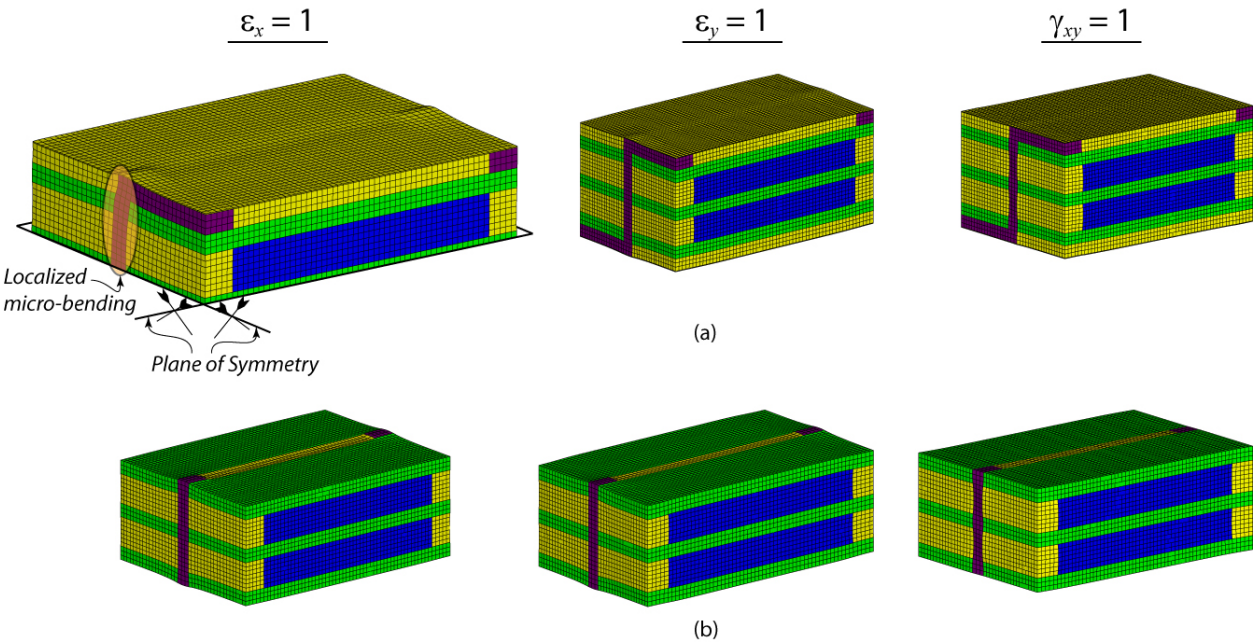

Figure 3: Deformed configurations of the unit-cells of the materials modeled in this study. The first, second and third column of meshes correspond to deformed configurations under macro-level unit-strains $\varepsilon_x = 1$, $\varepsilon_y = 1$, $\gamma_{xy} = 1$, respectively. (a) Z-Crowned Composite. For $\varepsilon_x = 1$, merely the top half of the unit-cell is shown in order to highlight the severe micro-bending of the Z-yarns. (b) Uncrowned Composite.

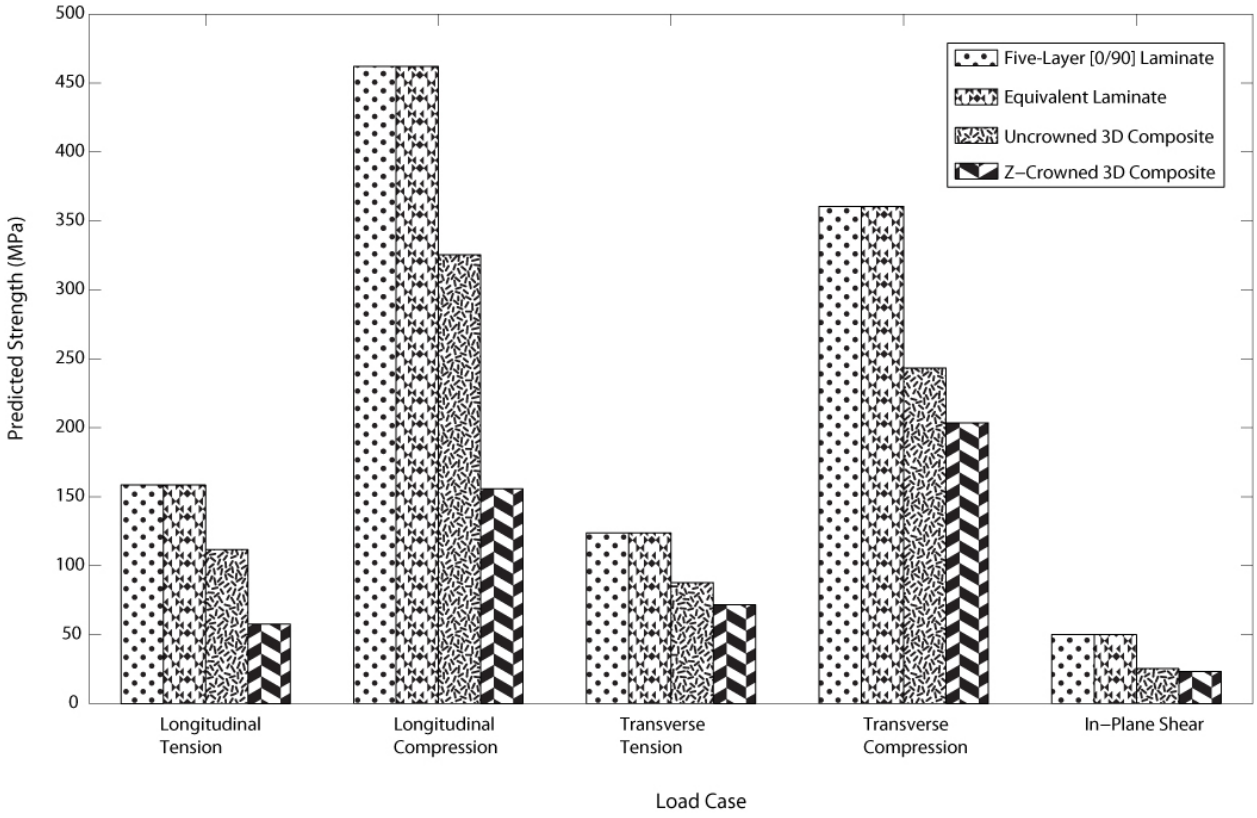

Figure 4: In-plane strengths of the 'Five-Layer [0/90] Laminate', Equivalent Laminate, Uncrowned Composite and the Z-Crowned Composite, under different loading cases. The strength of the 'Five-Layer [0/90] Laminate' was predicted based on Classical Lamination Theory, whereas, the strengths of the other material configurations were predicted in accordance with the One Element failure threshold, for individual loading cases.

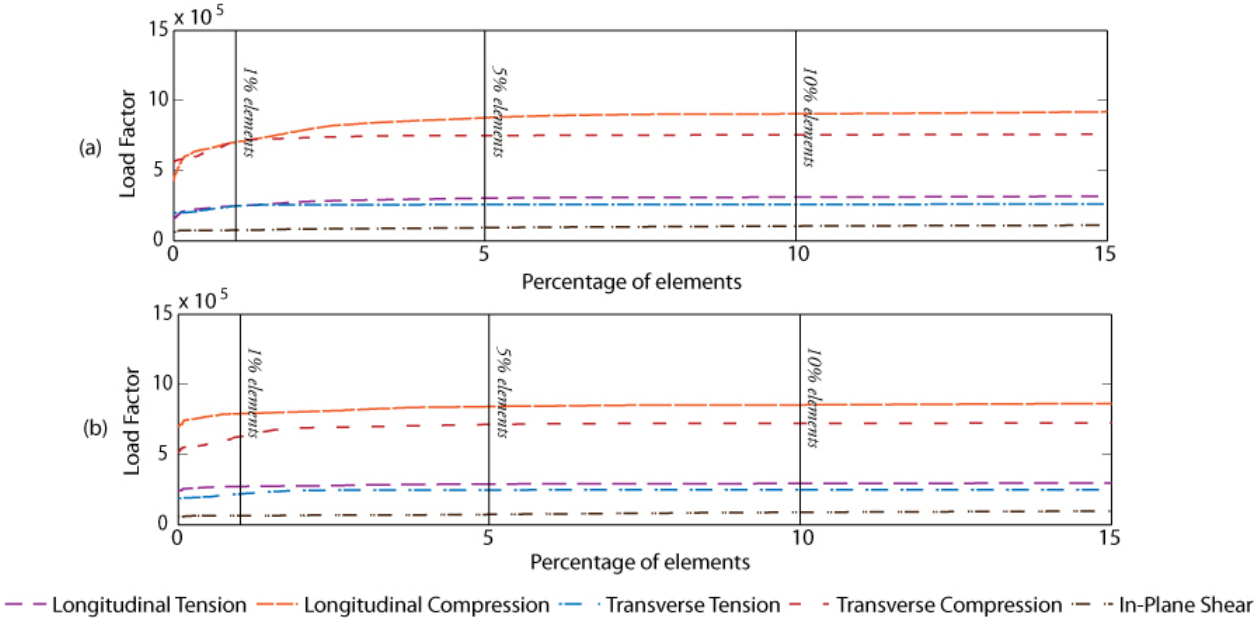

Figure 5: Detailed inspection of the load factors of 15% of the elements in individual finite element meshes sorted in ascending order. (a) Z-Crowned composite. (b) Uncrowned composite.

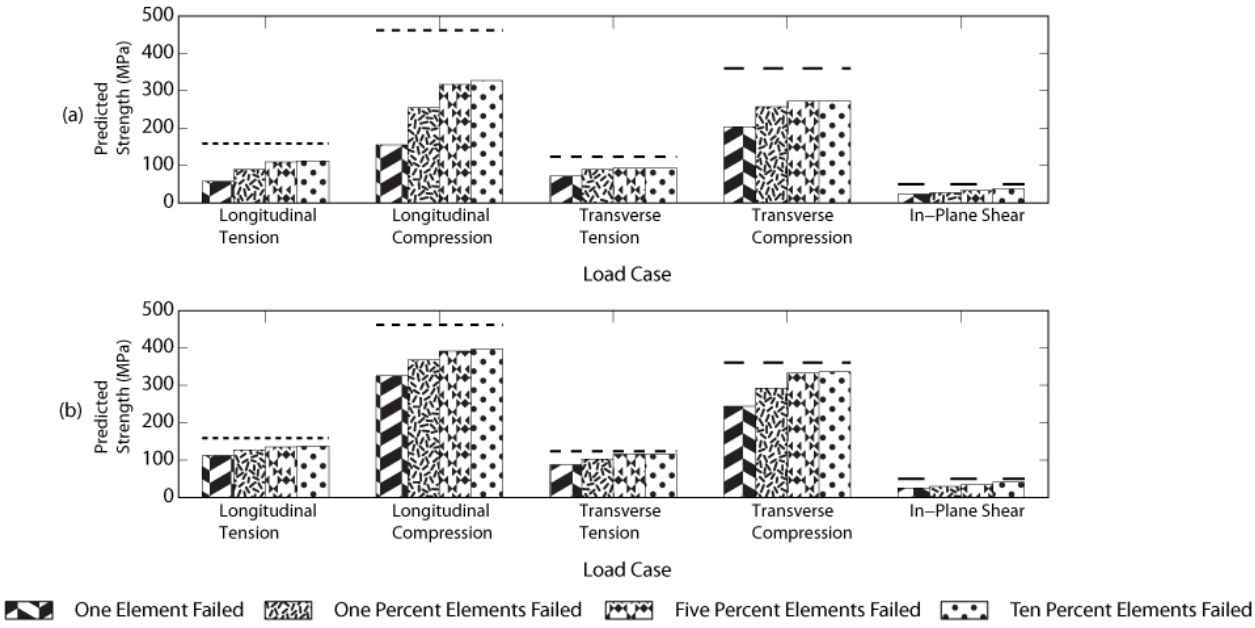

Figure 6: Variation in the planar strengths of the three materials modeled in this study. The dashed horizontal lines represent the strengths of the Equivalent Laminate for individual loading cases. (a) Z-Crowned composite. (b) Uncrowned composite. These results were obtained based on choosing load factors corresponding to different levels of allowable element failure as shown in Figure 5.

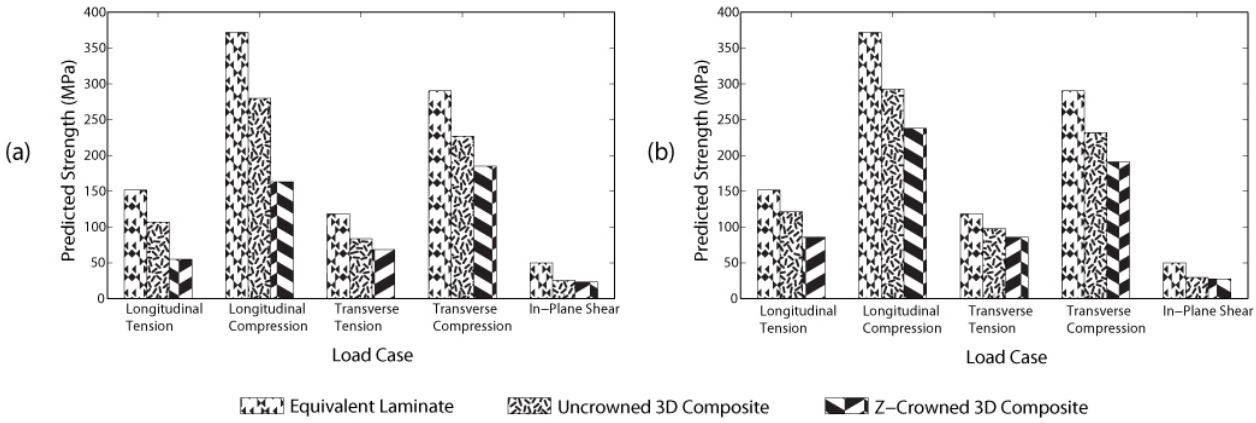

Figure 7: Strength knockdowns in the equivalent laminate, uncrowned composite and the Z-crowned composite based on different levels of allowable element failure. (a) One Element failure condition wherein the entire composite is assumed to have failed when the first element failure is encountered – most conservative threshold. (b) One percent of the elements are allowed to fail.

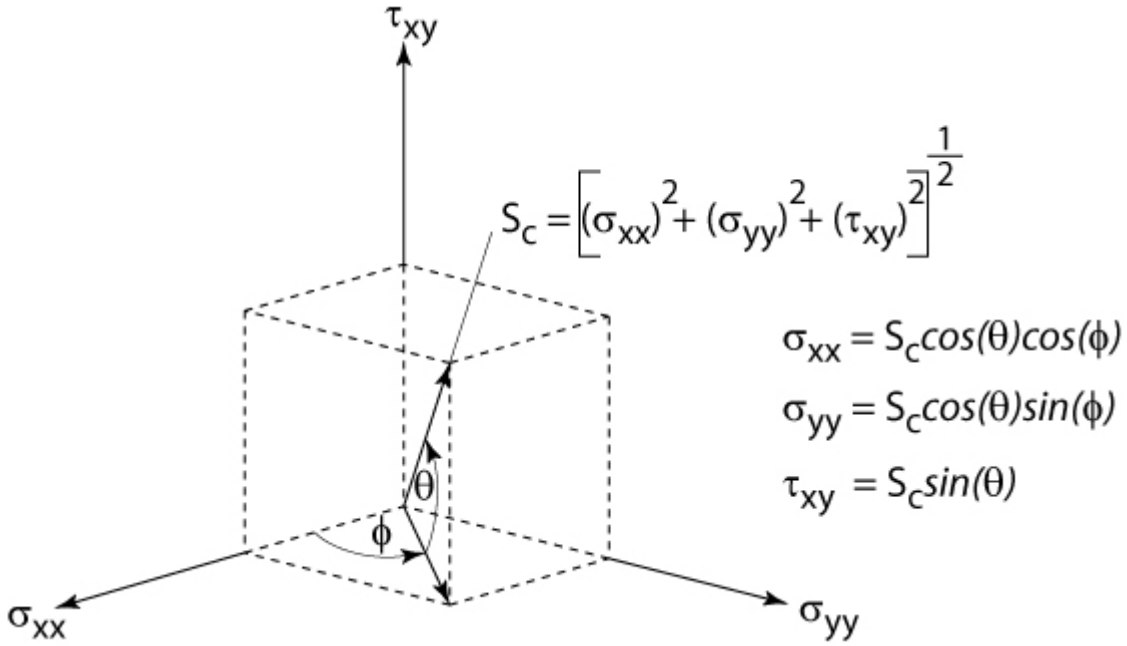

Figure 8: Representation of combined in-plane loading as functions of the Euler loading angles ϕ and θ.

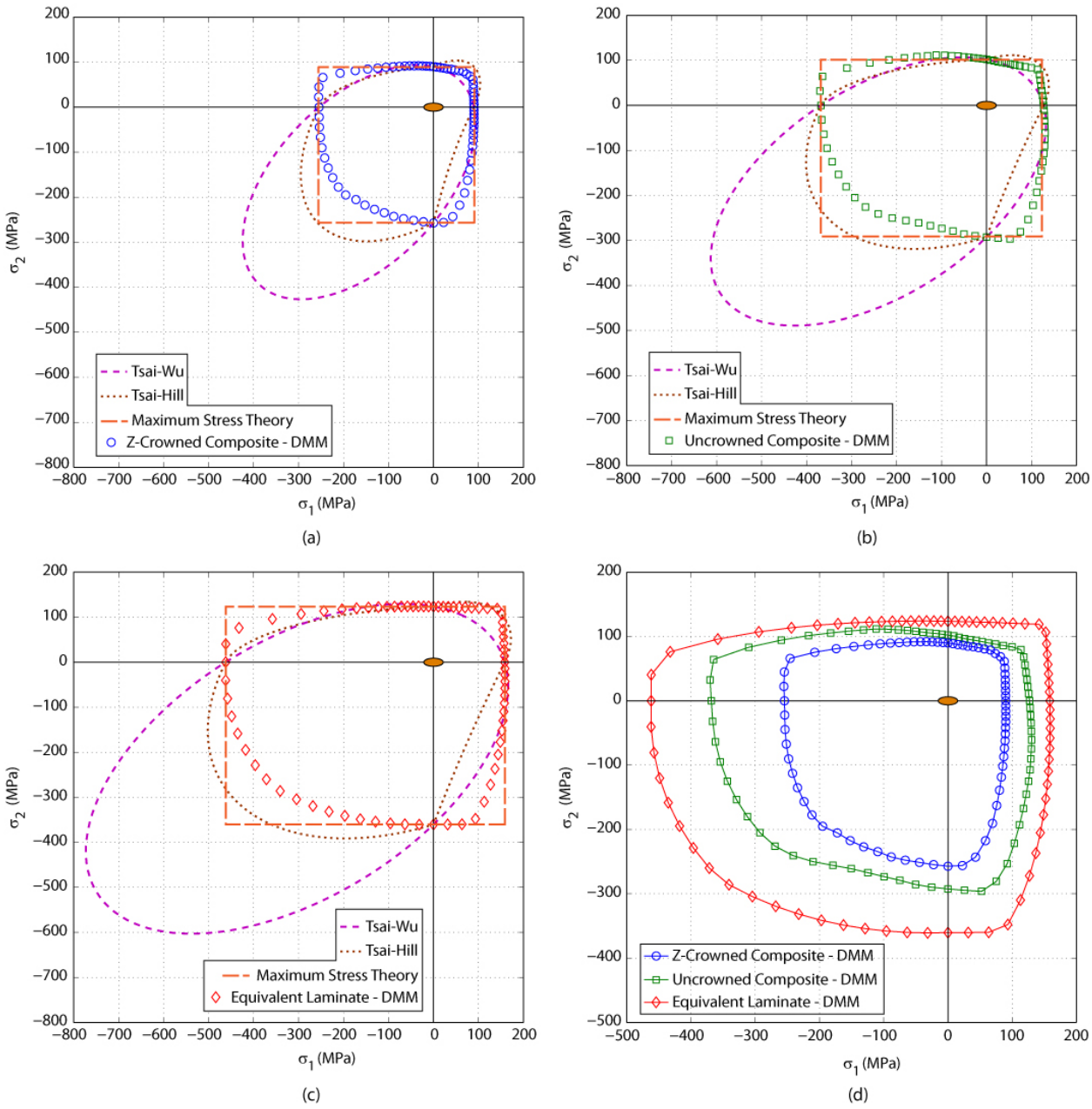

Figure 9: Failure loci and Direct Micro-Mechanics (DMM) based individual failure data points. (a) Z-Crowned Composite. (b) Uncrowned Composite. (c) Equivalent Laminate. (d) The DMM failure loci for the Z-Crowned Composite, Uncrowned Composite, and the Equivalent Laminate. With the introduction of the Z-yarns, the failure envelopes shrink progressively, indicating severe knockdowns in strengths.

Table 1: Dimensions of the tows and yarns employed to develop 3D models of the unit-cell of the weave architecture shown in Figure 1. The subscripts 'f', 'w', and 'z' indicate fill tows, warp tows and Z-yarns, respectively. The above dimensions were computed based on the work in [2]. *All dimensions are in mm*.

Geometry Parameters								
h_f	h_w	h_z	w_f	w_w	w_z	L	W	H
0.292	0.637	0.292	1.514	4.120	0.910	3.320	5.028	2.734

Table 2: Periodic boundary conditions applied on the unit-cells shown in Figure 2 for simulating in-plane unit-strain loading cases [14].

Load Case	*u(a/2,y,z) – u(-a/2,y,z)*	*v(a/2,y,z) – v(-a/2,y,z)*	*w(a/2,y,z) – w(-a/2,y,z)*	*u(x,b/2,z) – u(x,-b/2,z)*	*v(x,b/2,z) – v(x,-b/2,z)*	*w(x,b/2,z) – w(x,-b/2,z)*
$\varepsilon_x^M = 1$	*a*	*0*	*0*	*0*	*0*	*0*
$\varepsilon_y^M = 1$	*0*	*0*	*0*	*0*	*b*	*0*
$\gamma_{xy}^M = 1$	*0*	*a/2*	*0*	*b/2*	*0*	*0*

Table 3: Material properties of the transversely isotropic warp tows, fill tows and the Z-yarns [9].

All elastic and shear moduli are reported in GPa.								
E_{11}	E_{22}	E_{33}	ν_{12}	ν_{23}	ν_{13}	G_{12}	G_{23}	G_{13}
53.424	10.684	10.684	0.053	0.449	0.265	4.183	3.688	4.183
All strengths are reported in MPa.								
S_L^+		S_L^-		S_T^+		S_T^-		S_{LT}
1380		770		47		137		50

Table 4: The extensional stiffness matrices and effective elastic properties of 3D woven composites. Owing to the symmetry of the weave architecture about the mid-plane [B] ≈ [0]. Clearly the addition of Z-yarns results in significant knockdowns in the properties.

Weave Architecture	**[A] (MPa-m)**	E_{xx} **(GPa)**	E_{yy} **(GPa)**	ν_{xy}	ν_{yx}	G_{xy} **(GPa)**
Finite Element Solutions						
Z-Crowned Composite	$\begin{bmatrix} 69.61 & 2.57 & 0.00 \\ 2.57 & 57.61 & 0.00 \\ 0.00 & 0.00 & 8.61 \end{bmatrix}$	25.15	20.81	0.0447	0.0370	3.11
Uncrowned Composite	$\begin{bmatrix} 65.66 & 1.75 & 0.00 \\ 1.75 & 54.91 & 0.00 \\ 0.00 & 0.00 & 7.60 \end{bmatrix}$	30.51	25.52	0.0318	0.0266	3.35
Equivalent Laminate	$\begin{bmatrix} 77.60 & 1.22 & 0.00 \\ 1.22 & 60.50 & 0.00 \\ 0.00 & 0.00 & 8.99 \end{bmatrix}$	36.10	28.13	0.0202	0.0157	4.183
Analytical Solution						
Five-Layer [0/90] Laminate	$\begin{bmatrix} 77.47 & 1.21 & 0.00 \\ 1.21 & 60.45 & 0.00 \\ 0.00 & 0.00 & 8.99 \end{bmatrix}$	36.02	28.10	0.0202	0.0157	4.183

Table 5: Comparison of longitudinal (E_{xx}) and transverse (E_{yy}) elastic moduli reported in [2,9] with corresponding results obtained in the present study. The predictions obtained from the current analyses are in reasonably good agreement with published data within the realm of numerical uncertainty.

Model	E_{xx} **(GPa)**	E_{yy} **(GPa)**	$E_{xx}^{Experimental}$ **(GPa)**	$E_{yy}^{Experimental}$ **(GPa)**
Ref [2]	27.31	25.70	24.68	20.75
Ref [9]	27.90	26.20	NA	
Uncrowned Composite	30.51	25.52		
Z-Crowned Composite	25.15	20.81		

Table 6: Predicted in-plane longitudinal, transverse and shear strengths for the three material configurations investigated in this study. The results indicate significant increases in predicted strengths for the Uncrowned Composite and the Z-Crowned Composite as the failure threshold is increased from the One Element level to the 1% allowable element failure condition. The predicted strengths for the Equivalent Laminate do not change with failure threshold as discussed previously.

Failure Threshold	$S_{L(+)}^{FEA}$ **(MPa)**	$S_{L(-)}^{FEA}$ **(MPa)**	$S_{T(+)}^{FEA}$ **(MPa)**	$S_{T(-)}^{FEA}$ **(MPa)**	S_{LT}^{FEA} **(MPa)**
Z-Crowned Composite					
One Element	57.51	155.73	71.58	203.61	23.24
1 Percent Elements	89.86	254.50	89.82	257.17	27.40
% Increase	56.25	63.42	25.48	26.30	17.90
Uncrowned Composite					
One Element	111.70	325.40	87.65	243.36	25.35
1 Percent Elements	126.86	368.29	102.06	292.49	29.62
% Increase	13.57	13.18	16.44	20.18	16.84
Equivalent Laminate					
One Element	158.52	462.00	123.70	360.44	50.00
1 Percent Elements	158.52	462.00	123.70	360.44	50.00

Table 7: Comparison of longitudinal and transverse tensile strengths of the 3D woven composites studied in [2] and the present work. The results from [2] reported herein are based on the initial failure strain $\varepsilon_x^{iT} = 0.554\%$.

Model	$\boldsymbol{S_{L(+)}}$ **(MPa)**	$\boldsymbol{S_{T(+)}}$ **(MPa)**
Ref [2] – Theoretical	151.00	NA
Ref [2] – Experimental	140.00	NA
Uncrowned Composite	126.86	102.06
Z-Crowned Composite	89.86	89.82

Table 8: The knockdown in the predicted strength of the 3D woven composite studied in this work. The individual strength magnitudes of the Uncrowned Composite and Z-Crowned Composite for comparison with the Equivalent Laminate are based on the 1 Percent element failure condition reported in Table 6. The 'Ref [2] – Theoretical' and 'Ref [2] – Experimental' strength magnitudes for comparison with the Equivalent Laminate are given in Table 7

Percentage Knockdown					
Model	$\boldsymbol{S_{L(+)}}$	$\boldsymbol{S_{L(-)}}$	$\boldsymbol{S_{T(+)}}$	$\boldsymbol{S_{T(-)}}$	$\boldsymbol{S_{LT}}$
Ref [2] – Theoretical	5%	NA	NA	NA	NA
Ref [2] – Experimental	12%	NA	NA	NA	NA
Uncrowned Composite	20%	20%	18%	19%	41%
Z-Crowned Composite	43.31%	45%	28%	29%	45%